CHEMISTRY OF MATERIALS
Cite This: Chem. Mater. 2018, 30, 1585−1592
Article
pubs.acs.org/cm

Growth of Nanoparticles with Desired Catalytic Functions by Controlled Doping-Segregation of Metal in Oxide

Qiyuan Wu,[†,○] Binhang Yan,[‡,§,○] Jiajie Cen,[†,○] Janis Timoshenko,[†] Dmitri N. Zakharov,[∥] Xianyin Chen,[⊥] Huolin L. Xin,[∥] Siyu Yao,[‡] John B. Parise,[⊥,#] Anatoly I. Frenkel,[†,‡] Eric A. Stach,[∥,▽] Jingguang G. Chen,[*,‡,^] and Alexander Orlov[*,†]

[†]Department of Material Science and Chemical Engineering, Stony Brook University, Stony Brook, New York 11794, United States
[‡]Chemistry Department, Brookhaven National Laboratory, Upton, New York 11973, United States
[§]Department of Chemical Engineering, Tsinghua University, Beijing 100084, China
[∥]Center for Functional Nanomaterials, Brookhaven National Laboratory, Upton, New York 11973, United States
[⊥]Chemistry Department, Stony Brook University, Stony Brook, New York 11794, United States
[#]Department of Geosciences, Stony Brook University, Stony Brook, New York 11794, United States
[▽]Department of Materials Science and Engineering, University of Pennsylvania, Philadelphia, Pennsylvania 19104, United States
[^]Department of Chemical Engineering, Columbia University, New York, New York 10027, United States

Supporting Information

ABSTRACT: The size and morphology of metal nanoparticles (NPs) often play a critical role in defining the catalytic performance of supported metal nanocatalysts. However, common synthetic methods struggle to produce metal NPs of appropriate size and morphological control. Thus, facile synthetic methods that offer controlled catalytic functions are highly desired. Here we have identified a new pathway to synthesize supported Rh nanocatalysts with finely tuned spatial dimensions and controlled morphology using a doping-segregation method. We have analyzed their structure evolutions during both the segregation process and catalytic reaction using a variety of in situ spectroscopic and microscopic techniques. A correlation between the catalytic functional sites and activity in CO_2 hydrogenation over supported Rh nanocatalysts is then established. This study demonstrates a facile strategy to design and synthesize nanocatalysts with desired catalytic functions.

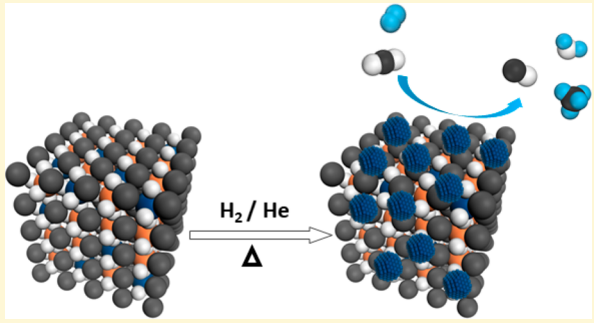

INTRODUCTION

The structural properties of metal nanoparticles (NPs), including size and morphology, often play a critical role in defining the catalytic performance (e.g., activity, selectivity, and stability) of supported metal nanocatalysts.[1−4] Common synthetic methods such as wet impregnation involve two steps: attaching the metal precursors to support materials followed by a reduction process to convert the precursors to metal NPs.[5] However, these approaches offer limited control over the size and morphology of the metal NPs during the reduction and/or during catalytic reaction.[6−8] In order to better control the size and morphology of metal NPs, different approaches have been developed. These frequently employ capping or encapsulating agents during chemical synthesis[3,9−11] or apply size control processes during physical deposition.[12,13] Although these approaches have been shown to better control the size and morphology of NPs, they have their own significant drawbacks. For instance, capping and encapsulating agents are usually difficult to remove completely, resulting in surface contamination, and physical deposition methods have so far proven to be impractical when scaled up for industrial applications.[14,15] Thus, there is a continued need for facile synthetic methods that offer controlled fabrication of nanocatalysts with desired catalytic functions for use in practical catalytic applications.

A possible way forward can be inspired by the work of Akao et al. where they demonstrated that Pd atoms could be doped into the lattice of perovskite oxides (ABO_3) during the synthesis of the oxide and subsequently segregated to the surface to form Pd NPs during reduction process.[16] Such a doping-segregation method represents a simple synthetic process, which may offer significant industrial advantages in catalyst synthesis and immobilization. Despite subsequent efforts by other groups to better understand the doping-segregation process and its application for nanocatalyst preparation, only limited progress has been made. For example,

Received: November 8, 2017
Revised: January 31, 2018
Published: February 5, 2018

DOI: 10.1021/acs.chemmater.7b04699
Chem. Mater. 2018, 30, 1585−1592

Tanaka et al. compared the segregation behavior of different precious metals in different perovskite oxides by applying ex situ X-ray absorption fine structure (XAFS) analysis. They found that both the type of dopant atoms and the choice of perovskite oxide had significant effects on the segregation process.[17] Recently, Irvine et al. demonstrated that the stoichiometry of perovskite oxides could also control the segregation of dopant atoms[6] and produced Ni nanocatalysts with excellent stability for the methane reforming reaction.[8] Despite these important findings, many questions about the doping-segregation process and the structure-performance correlation of the produced catalysts remain unanswered. Detailed investigation on structure evolution during the segregation process applying in situ characterization techniques is still lacking. Furthermore, it is unclear whether it is possible to tune the size of formed NPs while maintaining a similar morphology because of the lack of fundamental understanding of the segregation process. In addition to the segregation process, it is also critical to explore these aspects from a practical perspective, so as to develop a clear understanding on how to tune the doping-segregation method to improve the activity and selectivity of the catalysts.

Here we present a systematic investigation on the segregation behavior of Rh dopant atoms in Rh-doped $SrTiO_3$ from different perspectives, employing in situ structural characterization techniques, including X-ray diffraction (XRD), environmental transmission electron microscopy (E-TEM), and XAFS, to first study the onset temperature of Rh segregation. We then demonstrated that, by modulating the reduction temperature, the size of the formed Rh NPs can be precisely tuned within a small range (1.1 to 2.2 nm). Finally, by conducting catalytic CO_2 hydrogenation as a model catalytic reaction and utilizing in situ diffuse reflectance infrared Fourier transform spectroscopy (DRIFTS) for characterization of surface intermediates, we showed that the morphology of formed Rh NPs of different sizes remained similar and established a correlation between catalytic functional sites and activity in CO_2 hydrogenation reaction over supported Rh nanocatalysts. Our results highlight a simple yet effective way to produce Rh nanocatalysts with controlled size and morphology. Important insights into the understanding of the doping-segregation process and the structure-performance correlation described in this work could guide the preparation of other catalysts with desired functional sites based on this synthetic method.

RESULTS AND DISCUSSION

Several characterization techniques were employed to understand the catalyst structure. The crystalline phase of synthesized Rh-doped $SrTiO_3$ was first confirmed by ex situ XRD. The XRD patterns of synthesized pristine $SrTiO_3$ (HT-0) and Rh-doped $SrTiO_3$ (HT-4 and HT-10) samples are shown in the inset of Figure 1 along with the standard diffraction pattern of $SrTiO_3$ (JCPDS No. 35-0734). The samples exhibited diffraction patterns typical for those of cubic perovskite structures,[18−20] with the highest intensity diffraction peak corresponding to the (110) plane reflection. Following the confirmation of the cubic perovskite structure of synthesized Rh-doped $SrTiO_3$, the evolution of the $SrTiO_3$ lattice during the reductive segregation of Rh was investigated by in situ XRD measurements. Figure 1 shows the lattice size of the Rh-doped $SrTiO_3$ sample during reduction under a 4% H_2 flow as a function of temperature. The lattice parameter of the Rh-doped

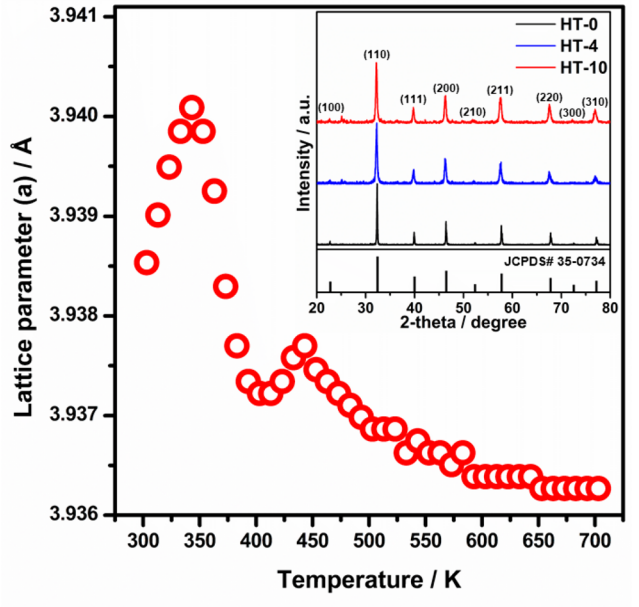

Figure 1. Evolution of lattice size of Rh-doped $SrTiO_3$ during reductive heating. Inset shows the diffraction patterns for synthesized pristine $SrTiO_3$ (HT-0) and Rh-doped $SrTiO_3$ (HT-4 and HT-10) samples along with the standard diffraction pattern of $SrTiO_3$. The only weak reflection that could not be attributed to the perovskite was assigned to the trace amount of TiO_2 precursor. The lattice parameter of the cubic perovskite structure of the Rh-doped $SrTiO_3$ sample was calculated from the position of (110) plane reflection.

$SrTiO_3$ was calculated from the (110) plane reflection. The data show that, during the temperature ramping, the lattice of Rh-doped $SrTiO_3$ initially expanded, followed by fast contracting which ended at ∼573 K. The expansion of the lattice can be attributed to thermal expansion, while the shrinkage of lattice indicated the segregation of Rh dopant atoms to the surface of Rh-doped $SrTiO_3$.[17,21] The stability of the perovskite structure at the temperatures above the ones used for in situ XRD experiments (e.g., above 700 K) was also evaluated by ex situ XRD. The samples subjected to reducing and oxidizing high-temperature treatments at 973 K retained cubic perovskite structure as shown in Figure S1 in the Supporting Information, SI.

In order to visualize the segregation of Rh dopant atoms and subsequent formation of Rh NPs on the surface of $SrTiO_3$ during the reduction, TEM characterization was carried out following the in situ XRD investigation. The cubic perovskite structure of synthesized Rh-doped $SrTiO_3$ (HT-4) was again confirmed by lattice fringe analysis of ex situ high-resolution TEM (HRTEM) images (Figure S2a in the SI). In order to have a more detailed understanding of the formation of Rh NPs, in situ E-TEM imaging of the samples was performed. Figure 2 shows in situ HRTEM images of a Rh-doped $SrTiO_3$ (HT-4) particle obtained during sample exposure to 1 Torr of H_2 at the indicated temperatures. At 300 K, no Rh NPs were observed, as shown in Figure 2a, consistent with the XRD results. The effect of temperature on NP formation was then probed by taking HT-4 to elevated temperatures (Figure 2b−d, 373, 473, and 573 K, respectively). The attained images provide clear evidence of NP formation at 573 K, agreeing well with the in situ XRD results presented in Figure 1. In addition to confirming the formation of NPs during reduction at 573 K, Figure 2d shows that the formed NPs were evenly spaced. Such

DOI: 10.1021/acs.chemmater.7b04699
Chem. Mater. 2018, 30, 1585−1592

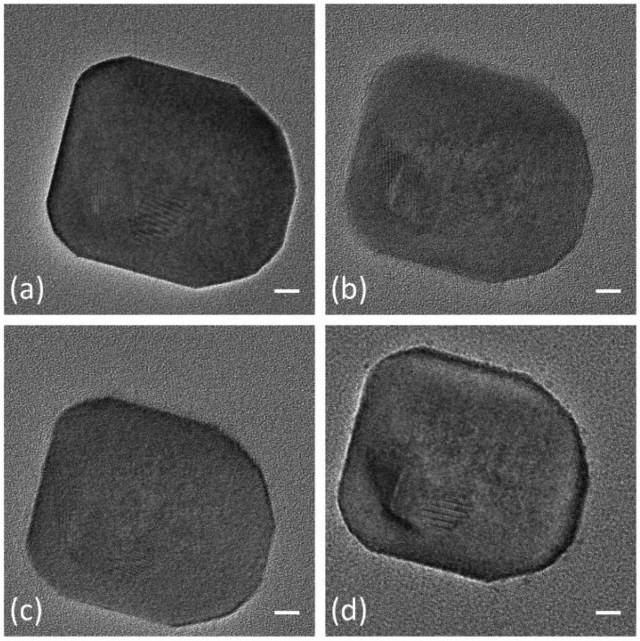

Figure 2. In situ TEM images of Rh-doped $SrTiO_3$ sample (HT-4) exposed to 1 Torr of H_2 at (a) 300, (b) 373, (c) 473, and (d) 573 K. Scale bar: 5 nm.

uniform dispersion of NPs is expected given that the lattice of $SrTiO_3$ is highly symmetric,[22] implying that the diffusivities of Rh atoms in the $SrTiO_3$ particle along all different directions are very similar. HRTEM images collected ex situ confirmed that the NPs observed were Rh NPs (Figure S2b in the SI).

Further confirmation of surface segregation of Rh species due to reductive heating was sought using STEM-EDS. Figure 3 presents high angle annular dark field (HAADF) images and the corresponding EDS elemental maps of reduced Rh-doped $SrTiO_3$ sample (HT-4-R). The elemental maps of Sr, Ti, and O have a high degree of uniformity, indicating that Sr, Ti, and O are evenly distributed over the entire $SrTiO_3$ particle and providing further confirmation of $SrTiO_3$ phase presence (Figure 3c–f). Rh mapping showed notable Rh atom segregation, resulting in the formation of Rh NPs (Figure 3b,f). In addition to confirming Rh segregation, the EDS analysis also highlights a need to address the following two questions: (1) what is the percentage of Rh atoms that have segregated to form NPs and (2) what is the pathway for controlling the degree of reductive segregation of Rh dopant atoms and the resulting size of Rh NPs.

Aiming at a better understanding of the segregation behavior of Rh dopant in the $SrTiO_3$ lattice and further answering these two questions, in situ XAFS measurements at the Rh K-edge for the Rh-doped $SrTiO_3$ samples (HT-4 and HT-10) were carried out. Evaluation (Figure S3a,b in the SI) for as-synthesized samples clearly demonstrates a nonmetallic state of Rh, while the local environment of Rh is different from that of Rh in Rh_2O_3. More specifically, the peak at 3.2 Å (Figure S3b in the SI) has its origin in Rh−O−Ti collinear linkage (vide infra), consistent with Rh dopant atoms substituting Ti atoms in the $SrTiO_3$ lattice[22,23] rather than forming Rh_2O_3. Overall, the XAFS results are consistent with Rh being homogeneously doped into the $SrTiO_3$. In contrast to as-synthesized sample data, results for samples subjected to in situ reduction (Figure S3c,d in the SI) indicate that all reduced samples contained a fraction of metallic Rh, consistent with the previously described STEM-EDS results. To facilitate data interpretation, it is important to highlight that, based on our initial experiments evaluating the effect of reduction time on Rh K-edge data (Figure S4), the reduction process was completed within 30 min.

Following the initial evaluation of XAFS data, a detailed analysis of both X-ray near edge absorption structure (XANES) and extended X-ray absorption fine structure (EXAFS) was performed. The XANES data for as-synthesized (HT-4 and HT-10) and reduced (HT-4-R and HT-10-R) samples, together with the reference data for Rh foil, are presented in Figure 4a,b. The samples showed the presence of multiple isosbestic points in the XANES region, suggesting that the reduced samples contained a two-phase mixture of Rh-doped $SrTiO_3$ and metallic Rh NPs. The molar fractions of each phase were obtained using a linear combination fitting analysis, revealing that about 64% of the Rh atoms were in the metallic

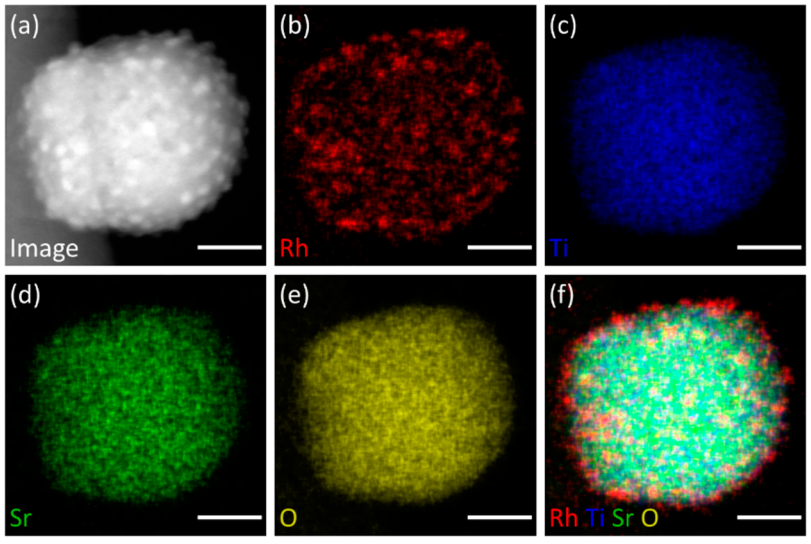

Figure 3. STEM images and EDS elemental maps of reduced Rh-doped $SrTiO_3$ sample (HT-4-R). (a) HAADF image of the sample; (b) Rh map, (c) Ti map, (d) Sr map, (e) O map, and (f) overlapped map. Scale bar: 10 nm.

DOI: 10.1021/acs.chemmater.7b04699
Chem. Mater. 2018, 30, 1585−1592

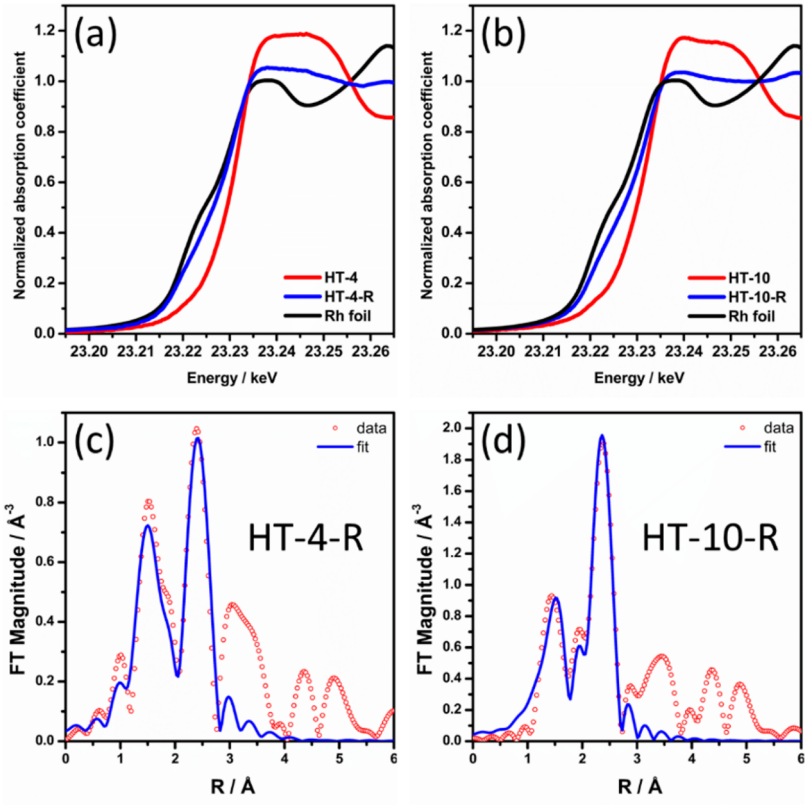

Figure 4. In situ XAFS data of Rh-doped $SrTiO_3$ samples. (a and b) XANES data of as-synthesized samples (HT-4 and HT-10), reduced samples (HT-4-R and HT-10-R), and Rh foil. (c and d) Fourier transform magnitudes of the k^2-weighted EXAFS data and results of fitting with theoretical model for reduced samples. All XAFS data were collected under 5% H_2 flow.

Rh NP phase for both samples, in line with literature values.[17] EXAFS analysis was applied to determine the local structure of Rh atoms in each phase. The experimental EXAFS data and results from fitting the data with theoretical models for reduced samples are shown in Figure 4c,d, and the estimated local structure parameters are given in Table 1. For all samples, the amplitude reduction factor (0.86) was obtained from fitting of EXAFS data for Rh foil with the known first nearest neighbor coordination number (12, Figure S5 in the SI) and was later fixed to that value (0.86) to determine the coordination number (CN) values for other samples. It is important to highlight that for substitutionally doped $SrTiO_3$, where Rh substitutes Ti, the first shell coordination number for Rh coordinated with O is 6. Correspondingly, any decrease in CN observed in the reduced samples would indicate the presence of Rh atoms residing outside of the $SrTiO_3$ lattice (Table 1).

Table 1. Local Structure Parameters for Rh Atoms in Reduced Samples Estimated from EXAFS Analysis

samples	shells	CN (corrected)	bond length[a]/Å	estimated size[b]/nm
HT-4-R	Rh−O	1.7 (4.7)	2.01	1.1
	Rh−Rh	4.2 (6.6)	2.69	
HT-10-R	Rh−O	1.8 (5)	1.95	2.2
	Rh−Rh	6.4 (10)	2.67	

[a]For reference, the bond length of Ti−O bond in the ideal $SrTiO_3$ lattice is 1.95 Å, and the bond length of Rh−Rh bond in Rh metal is 2.68 Å. [b]Estimated using corrected CN based on a model from published literature.[24]

Furthermore, by dividing the CN by 6, it is possible to estimate that around 30% of Rh atoms remain in the $SrTiO_3$ lattice given that Rh atoms in the metallic phase would not contribute to any Rh−O scattering in the EXAFS data. This estimate is consistent with that obtained from the XANES data, further supporting the results of the EXAFS analysis. The molar fraction of Rh atoms remaining in the substitutionally doped state obtained from XANES data was used to correct the ensemble Rh−Rh CNs obtained from the EXAFS analysis and determine the NP-specific Rh−Rh CNs (Table 1). The average size of Rh NPs produced during the reductive segregation was estimated using the NP-specific CN for each sample (Table 1), while assuming the face-center cubic (fcc) structures for Rh NPs.[24] The assumption of Rh NPs shapes was based on ex situ TEM images (Figure S6a,c in the SI), and the estimated particle size was consistent with that obtained from the ex situ TEM images (Figure S6b,d in the SI).

With the segregation behavior of Rh dopant in the $SrTiO_3$ lattice established, a method for precisely tuning the Rh NP size using temperature modulation was sought. In situ XANES experiments were performed during the reduction of the Rh-doped $SrTiO_3$ samples (HT-4) in a 5% H_2 flow at different temperatures. The XANES results indicated that the fraction of metallic Rh NP phase increased monotonically with an increase in the reduction temperature from 573 to 973 K (Figure 5a and second entry in Table S1 in the SI). As the fraction of metallic Rh NPs increased, one would also expect the particle size of these NPs to increase. To confirm this trend, ex situ TEM imaging (Figure S7) of the reduced samples was conducted. Figure 5b presents the particle size distributions of Rh NPs for samples reduced at different temperatures. The average Rh NP

DOI: 10.1021/acs.chemmater.7b04699
Chem. Mater. 2018, 30, 1585−1592

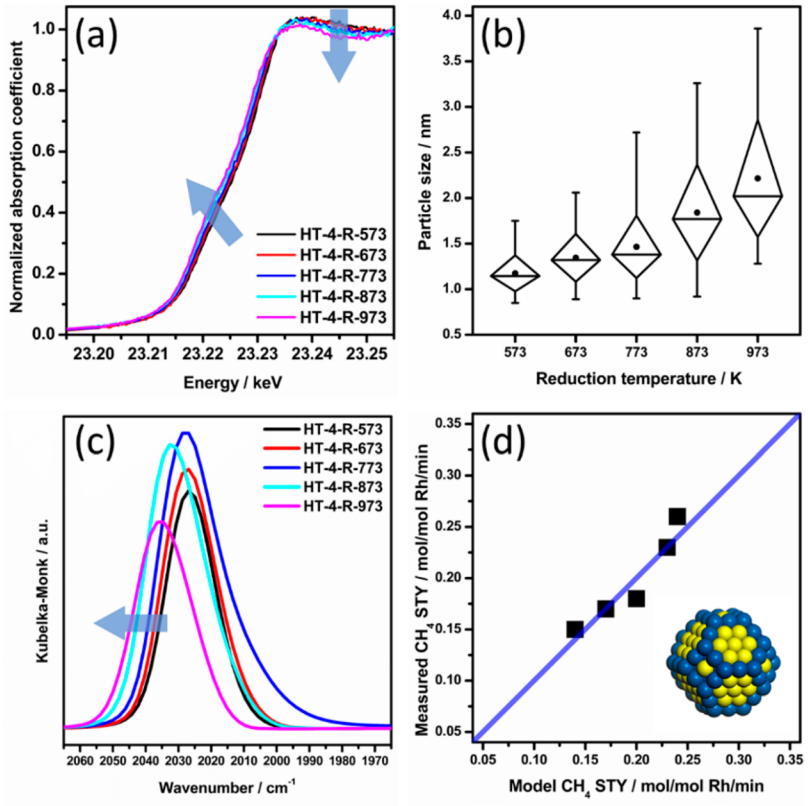

Figure 5. In situ XANES spectra (a) and box graphs of particle size distribution based on ex situ TEM images (b) of Rh NPs for Rh-doped $SrTiO_3$ samples (HT-4) reduced at different temperatures. Arrows in (a) indicate the direction of increasing reduction temperatures. (c) In situ DRIFT spectra of linear CO bond on Rh NPs at 573 K for Rh-doped $SrTiO_3$ samples (HT-4) reduced at different temperatures. The arrow in (c) indicates the wavenumber shift direction for increasing reduction temperatures. (d) Parity plot for the results obtained in the model described for the catalysts. The line indicates the case of perfect matching between experimental data and calculated data. Inset in (d) shows a model particle where the edge sites are highlighted in blue color and face sites are highlighted in yellow color. Number X in annotation "HT-4-R-X" represents the reduction temperature (K).

size was found to increase monotonically from 1.1 ± 0.2 to 2.2 ± 0.6 nm as the reduction temperature was increased from 573 to 973 K, respectively, indicating that temperature can be used as a single variable to precisely tune the Rh NP size.

To demonstrate that the controlled segregation not only allows tuning of Rh NP size but also preserves the morphology of Rh NPs, the Rh-doped $SrTiO_3$ samples (HT-4) reduced at different temperatures were tested for catalytic CO_2 hydrogenation. The catalytic testing results are summarized in Table 2, with the additional details presented in Figure S8 and Table S1 in the SI. A physical model (inset in Figure 5d and Scheme S1) representing a specific morphology[25−27] of Rh NPs was then constructed to calculate the space-time yield (STY) of methane from CO_2 hydrogenation. The model was based on the morphology of Rh NPs as indicated by TEM images (Scheme S1). The calculations for methane STY assumed the existence of two different types of active sites (i.e., edge sites and face sites) on the surface of the NPs with the number of atoms for each site being a function of the size of NPs. Additional details are provided in the SI. This model suggests that the Rh NPs of similar morphology but different particle size should show different fractions of surface sites. The larger the particle size, the lower the fraction of edge sites on the NP surface.[25] To validate this model, we first studied the adsorption behavior of CO on Rh NPs, a critical intermediate step in the CO_2 hydrogenation reaction.[28] More specifically, the adsorption configuration of CO on Rh NPs was investigated by

Table 2. Summary of Flow Reactor Data for Catalytic CO_2 Hydrogenation Reaction (1:1 Ratio, 2 mL/min CO_2 + 2 mL/min H_2 + 36 mL/min Ar) at 573 K[a]

catalyst		HT-4				
reduction temperature/K		573	673	773	873	973
conversion/%	CO_2	10.05	10.97	11.64	10.74	6.73
	H_2	13.37	13.92	13.99	12.91	8.75
yield/ % (carbon basis)	CO	8.69	9.64	10.50	9.72	5.83
	CH_4	1.08	1.00	0.86	0.89	0.86
TOF/ $mol/mol_{Rh}/min$	CO_2	1.79	1.95	2.07	1.91	1.20
	H_2	2.55	2.65	2.67	2.46	1.67
STY/ $mol/mol_{Rh}/min$	CO	1.56	1.73	1.88	1.74	1.05
	CH_4	0.19	0.18	0.15	0.16	0.15

[a]Values were calculated by averaging data points between 1-4 h on stream.

in situ DRIFTS, which showed that the doped samples (HT-4) reduced at different temperatures exhibited a single CO peak (between 2000 and 2050 cm^{-1}; Figure S9 in the SI). This peak can be assigned to a linear adsorption geometry of CO on Rh,[29] suggesting that Rh NPs formed under different reduction conditions still retain a comparable morphology. Furthermore, DFT calculations[30] suggest that the binding energy of CO linearly adsorbed on the edge sites of Rh NPs is larger than that on the face sites, which translates into a lower C−O stretching frequency. Combining the trend in Rh NP size evolution

DOI: 10.1021/acs.chemmater.7b04699
Chem. Mater. 2018, 30, 1585−1592

observed under TEM with the DFT calculations, one can expect that the C−O stretching frequency of linear Rh-CO adsorption would shift to higher wavenumbers with higher reduction temperatures, which was indeed confirmed with in situ DRIFTS spectra (Figure 5c). Given this validation, our proposed model of the Rh particle morphology was applied to methane STYs calculations. A parity plot representing the goodness of fit between experimental data and calculated data is shown in Figure 5d, showing a good match between experimental and model calculated data, indicating that the model with a specific morphology represents the NPs produced at different reduction temperature very well. Meanwhile, the calculated yield of methane on the edge sites was found to be ~1.6 times higher than that on the face sites, consistent with the difference between CO binding energies on the edge and face sites. Additional discussion is included in Table S1 in the SI. Lastly, we also evaluated the stability of Rh NPs before and after catalytic reaction. No significant sintering of Rh NPs was observed (Figure S10) indicating a fairly good stability of Rh NPs synthesized by the doping-segregation method.

CONCLUSION

In this work, the reductive segregation of Rh dopant atoms in Rh-doped $SrTiO_3$ was examined by various techniques to better understand this phenomenon and develop a pathway to finely tune Rh nanoparticle size with the aim of controlling their catalytic activity. In this pursuit, the controlled segregation of Rh dopant atoms enables the formation of Rh NPs with precisely tuned sizes within 1.1 to 2.2 nm, with well controlled morphology and catalytic activity. In situ XRD and E-TEM investigations revealed that the formation of Rh NPs on the surface of Rh-doped $SrTiO_3$ due to segregation of Rh dopant atoms started at the onset temperature of 573 K. Furthermore, in situ XAFS characterization suggested that the reductive segregation process could be controlled by varying the reduction temperature. Importantly, the controlled segregation produced Rh NPs with both finely tuned size and consistent morphology as revealed by a CO_2 hydrogenation probe reaction and in situ DRIFTS investigation. The results of this work highlight the significant potential of the doping-segregation method in producing nanocatalysts with controlled size and morphology. These results provide new insights into the contributions of different surface sites of Rh NPs to the methane yield of the CO_2 hydrogenation reaction. The results of this work demonstrate a facile strategy to design and produce nanocatalysts with desired catalytic functions.

EXPERIMENTAL METHODS

Synthesis. Rh-doped $SrTiO_3$ powder samples were synthesized by a hydrothermal (HT) method according to our previous report.[22] Strontium hydroxide octahydrate (Sigma-Aldrich; 95%), titanium dioxide (Sigma-Aldrich; nanopowder, 21 nm, 99.5%), and rhodium-(III) nitrate hydrate (Sigma-Aldrich; 36% rhodium basis) were used as the starting materials with a molar ratio of Sr/Ti/Rh = 1.10:(1 − x):x. In a typical synthesis to yield 1.468 g (4 mmol) of Rh-doped $SrTiO_3$ (1 mol % doped Rh), TiO_2 (0.316 g, 3.96 mmol) was suspended in 10 mL of deionized water. $Sr(OH)_2{\cdot}8H_2O$ (1.169 g, 4.4 mmol) was poured into the stirred suspension. $Rh(NO_3)_3$ (11.56 mg, 0.04 mmol) dissolved in 2 mL of deionized water was then added. The final suspension was sonicated for 30 min and then poured into a polytetrafluoroethylene (PTFE) lined stainless steel acid digestion vessel (model PA4749, volume 23 mL, Parr Instrument Company). The vessel was heated to 473 K at a rate of 2 K/min and then maintained at 473 K for 48 h. After cooling to room temperature, the vessel was opened, and the reaction product was centrifuged and washed several times with deionized water. The product was then dried at 353 K overnight. The samples with different Rh doping concentrations were denoted as HT-X, in which X represents X atom % of doped Rh. The samples reduced at 573 K were denoted as HT-X-R.

In Situ Characterization. *In Situ XRD Analysis.* In situ XRD analysis was carried out using of a Rigaku Ultima IV diffractometer (Cu Kα radiation, λ = 1.54056 Å) equipped with a D/TeX high-speed linear position sensitive detector), a Rigaku XRD-DSC stage, ULVAC vacuum pump, and a vacuum manifold. The desired atmosphere was achieved by controlling gas flows via selection manifold by utilizing mass flow controllers balancing the mixing of flow gases.[31] During the in situ XRD experiments, each powder sample was heated under in 4% H_2/He gas flow up to 723 K at a heating rate of 1 K/min. The XRD patterns were collected by at a rate of 0.01 degree/min with a 0.001-degree step size over the 2θ range from 31 to 34 degree.

E-TEM Imaging. Environmental TEM (E-TEM) imaging was conducted by using FEI Titan 80/300 E-TEM equipped with a postspecimen aberration corrector operating at 300 kV voltage. The corrector was tuned to a 20 mRad flat phase field. Powder samples were first suspended in ethanol and then drop-cast onto a Nano-Chip (DENSsolution). The Nano-Chip was then installed into an in situ heating holder (Wildfire, DENSsolution) for E-TEM imaging. One Torr of H_2 was introduced and maintained in the sample chamber in the microscope, and the sample was first imaged at 300 K. The sample was subsequently heated to specified temperatures in the presence of H_2 and then imaged at fixed temperature and pressure.

In Situ XAFS Studies. Rh K-edge (23230.23 eV) XAFS spectra for Rh-doped $SrTiO_3$ samples were acquired at SSRL beamline 2−2. Samples in powder form were mixed with boron nitride and pressed into pellets, which were then mounted in a Nashner-Adler cell[32] for heating and in situ XAFS measurements. For each of the samples three sets of XAFS spectra were acquired: for the as-synthesized sample at room temperature, for the sample heated for 30 min at 573 K, and for the sample cooled to room temperature. All measurements and sample heating were performed in a 5% H_2/He flow with a rate of 40 mL/min. Double crystal Si (220) monochromator was used for energy selection. X-ray beam size was 4 mm (horizontally) by 0.25 mm (vertically). Measurements were performed in transmission mode. XAFS spectra in bulk Rh foil, located between two ionization chambers downstream from the sample, were acquired in the same experiment and used as a reference material for absolute energy calibration and alignment purposes.

Rh K-edge XANES spectra for the Rh-doped $SrTiO_3$ (HT-4) sample under different reduction temperatures (from 573 to 973 K with 100 K increments) were also acquired. For this experiment, 20 mg of the HT-4 sample (60−80 mesh) were loaded into a 3 mm OD quartz tube, packed with quartz wool on both sides of the sample. The sample was reduced for 30 min at each temperature (i.e., 573, 673, 773, 873, and 973 K) in a 5% H_2/He flow. To avoid the thermal disturbance at high temperature, the spectra were collected after the sample was cooled down to room temperature in a 5% H_2/He flow. Measurements were performed in the fluorescence mode.

The experimental Rh K-edge XAFS spectra were extracted, aligned, and processed using conventional procedure using the Athena software[33] with the IFEFFIT package.[34] The EXAFS data were analyzed using the Artemis software within the IFEFFIT package.[34]

In Situ DRIFTS Analysis. In situ DRIFTS experiments were performed using an FTIR spectrometer (Thermo Nicolet 6700). Approximately 20 mg of fine catalyst powder was packed into the sample holder, and the surface was smoothly flattened to enhance IR reflection. With the cell securely located in the FTIR instrument, the catalyst was first reduced for 30 min at different temperatures (from 573 to 973 K with 100 K increments) in a 5% H_2 flow (20 mL/min). After cooling to 573 K, a background spectrum (512 scans) with a resolution of 4 cm^{-1} recorded in the mid-infrared range (650−4000 cm^{-1}) for each reduction temperature. Then the reactants, i.e., a 5% CO_2 + 5% H_2 mixture, with a total flow rate of 20 mL/min, were introduced into the cell. After 40 min of reaction, the CO_2/H_2 mixture

DOI: 10.1021/acs.chemmater.7b04699
Chem. Mater. 2018, 30, 1585−1592

was replaced by a 5% H_2 flow (20 mL/min) and purged for 30 min, and then the sample spectra (512 scans) were again collected.

Ex Situ Characterization. *Structure Characterization.* TEM imaging was conducted by using JEOL 2100F TEM operating at 200 kV voltage. The scanning transmission electron microscopy (STEM) and the energy-dispersive X-ray spectroscopy (EDS) data were acquired in an FEI Talos F200X S/TEM equipped with an extra-bright Schottkey field emission gun and a four-quadrant EDS detector. The instrument was operated at 200 kV voltage. Ex situ XRD data was acquired using a Rigaku Ultima III XRD diffractometer (Cu Kα radiation, λ = 1.54056).

CO Chemisorption. The surface Rh active sites were characterized by pulse CO chemisorption using an Altamira AMI-300ip instrument. The catalyst sample was dried for 30 min at 393 K in a He flow (30 mL/min), and subsequently reduced for 60 min at different temperatures (from 573 to 973 K with 100 K increments) using a mixture of 5% H_2 in Ar (30 mL/min). After reduction, the sample was purged with a 50 mL/min He flow for degassing. The reactor was then cooled to 313 K, and pulses of CO (59.0 μL) were passed over the catalyst until the CO peak area became constant. The amount of CO emerging from the reactor was monitored by a thermal conductivity detector (TCD). The CO uptake values are listed in Table S1.

Catalytic Reactions. Flow reactor studies of the CO_2 hydrogenation reaction were performed in a quartz tube reactor with an inner diameter of 4 mm under atmospheric pressure. ~20 mg of sieved catalyst (60−80 mesh) mixed with ~180 mg of inert material (acid-purified quartz precalcined at 1173 K for 2 h, 60−80 mesh) was loaded into a reactor tube and held in place by quartz wool. CO_2 and H_2 were set at 1:1 ratio (2 mL/min CO_2 with 2 mL/min H_2) and diluted with 36 mL/min Ar. Prior to each test at 573 K, the catalyst was first reduced for 60 min at different temperatures (from 573 to 973 K with 100 K increments) using a 5% H_2/Ar mixture (2 mL/min H_2 with 38 mL/min Ar). The inlet flow was then switched to reactants (2 mL/min CO_2, 2 mL/min H_2, and 36 mL/min Ar) and held for at least 4 h. The concentrations of gas products were analyzed online by gas chromatography (Agilent 7890B equipped with a flame ionization detector (FID) and a TCD). The conversion (X), yield (Y), selectivity (S), turnover frequency (TOF), and space-time yield (STY) were defined as

$$X_{CO_2} = \frac{F_{CO_2}^{inlet} - F_{CO_2}^{outlet}}{F_{CO_2}^{inlet}} \quad (1)$$

$$X_{H_2} = \frac{F_{H_2}^{inlet} - F_{H_2}^{outlet}}{F_{H_2}^{inlet}} \quad (2)$$

$$Y_{CO} = \frac{F_{CO}^{outlet}}{F_{CO_2}^{inlet}} \quad (3)$$

$$Y_{CH_4} = \frac{F_{CH_4}^{outlet}}{F_{CO_2}^{inlet}} \quad (4)$$

$$S_{CO} = \frac{Y_{CO}}{X_{CO_2}} \quad (5)$$

$$S_{CH_4} = \frac{Y_{CH_4}}{X_{CO_2}} \quad (6)$$

$$TOF_1 = \frac{F_{reactant}^{inlet} X}{U_{CO} W_{catalyst}}, \quad mol/mol_{site}/min \quad (7)$$

$$TOF_2 = \frac{F_{reactant}^{inlet} X}{L_{Rh} W_{catalyst}}, \quad mol/mol_{Rh}/min \quad (8)$$

$$STY_{product} = \frac{F_{product}^{outlet}}{L_{Rh} W_{catalyst}}, \quad mol/mol_{Rh}/min \quad (9)$$

$$STY_{product} = \frac{F_{product}^{outlet}}{W_{catalyst}}, \quad mol/g_{cat}/min \quad (10)$$

where F is the flow rate of reactant, mol/min; U_{CO} is the CO uptake value, μmol CO/g_{cat}; L_{Rh} is the loading amount of Rh, mol/g_{cat} which is 2×10^{-4} mol/g_{cat}; and W is the weight of catalyst used, g. The yields of both CO and CH_4 were controlled to be far away from the thermodynamic equilibrium limit.

■ ASSOCIATED CONTENT

Supporting Information

The Supporting Information is available free of charge on the ACS Publications website at DOI: 10.1021/acs.chemmater.7b04699.

Supporting figures and tables and details on the physical model applied in calculation of methane STY. (PDF)

■ AUTHOR INFORMATION

Corresponding Authors

*E-mail: jgchen@columbia.edu.

*E-mail: alexander.orlov@stonybrook.edu.

ORCID

Qiyuan Wu: 0000-0002-8751-2003

Anatoly I. Frenkel: 0000-0002-5451-1207

Eric A. Stach: 0000-0002-3366-2153

Jingguang G. Chen: 0000-0002-9592-2635

Author Contributions

The manuscript was written through contributions of all authors. All authors have given approval to the final version of the manuscript. These authors contributed equally.

Notes

The authors declare no competing financial interest.

■ ACKNOWLEDGMENTS

This research project has been supported by the NSF DMR Award 1254600. The research was carried out at Brookhaven National Laboratory (BNL) supported by the U.S. Department of Energy (DOE), Office of Science, Office of Basic Energy Sciences, Division of Chemical Sciences, Biosciences and Geosciences, under Contract DE-SC0012704. A.I.F. acknowledges support of the U.S. Department of Energy Grant No. DE-FG02-03ER15476 and Program Development funding at Brookhaven National Laboratory. This research used resources of the Center for Functional Nanomaterials, which is a U.S. DOE Office of Science Facility, at Brookhaven National Laboratory under Contract No. DE-SC0012704. Operations at the Beamline BL2-2 in SSRL were supported in part by the Synchrotron Catalysis Consortium (U.S. Department of Energy, Office of Basic Energy Sciences, Grant No. DE-SC0012335).

■ REFERENCES

(1) Subramanian, V.; Wolf, E. E.; Kamat, P. V. Catalysis with TiO2/Gold Nanocomposites. Effect of Metal Particle Size on the Fermi Level Equilibration. *J. Am. Chem. Soc.* **2004**, *126*, 4943−4950.

(2) Liu, Y.; Tsunoyama, H.; Akita, T.; Xie, S.; Tsukuda, T. Aerobic Oxidation of Cyclohexane Catalyzed by Size-Controlled Au Clusters on Hydroxyapatite: Size Effect in the Sub-2 nm Regime. *ACS Catal.* **2011**, *1*, 2−6.

DOI: 10.1021/acs.chemmater.7b04699
Chem. Mater. 2018, 30, 1585−1592

(3) Mostafa, S.; Behafarid, F.; Croy, J. R.; Ono, L. K.; Li, L.; Yang, J. C.; Frenkel, A. I.; Cuenya, B. R. Shape-Dependent Catalytic Properties of Pt Nanoparticles. *J. Am. Chem. Soc.* **2010**, *132*, 15714−15719.
(4) Reske, R.; Mistry, H.; Behafarid, F.; Roldan Cuenya, B.; Strasser, P. Particle Size Effects in the Catalytic Electroreduction of CO2 on Cu Nanoparticles. *J. Am. Chem. Soc.* **2014**, *136*, 6978−6986.
(5) Kim, J.-S.; Wieder, N. L.; Abraham, A. J.; Cargnello, M.; Fornasiero, P.; Gorte, R. J.; Vohs, J. M. Highly Active and Thermally Stable Core-Shell Catalysts for Solid Oxide Fuel Cells. *J. Electrochem. Soc.* **2011**, *158*, B596−B600.
(6) Neagu, D.; Tsekouras, G.; Miller, D. N.; Ménard, H.; Irvine, J. T. S. In situ growth of nanoparticles through control of non-stoichiometry. *Nat. Chem.* **2013**, *5*, 916−923.
(7) Wallace, W. T.; Min, B. K.; Goodman, D. W. The nucleation, growth, and stability of oxide-supported metal clusters. *Top. Catal.* **2005**, *34*, 17−30.
(8) Neagu, D.; Oh, T.-S.; Miller, D. N.; Ménard, H.; Bukhari, S. M.; Gamble, S. R.; Gorte, R. J.; Vohs, J. M.; Irvine, J. T. S. Nano-socketed nickel particles with enhanced coking resistance grown in situ by redox exsolution. *Nat. Commun.* **2015**, *6*, 8120.
(9) Cargnello, M.; Doan-Nguyen, V. V. T.; Gordon, T. R.; Diaz, R. E.; Stach, E. A.; Gorte, R. J.; Fornasiero, P.; Murray, C. B. Control of Metal Nanocrystal Size Reveals Metal-Support Interface Role for Ceria Catalysts. *Science* **2013**, *341*, 771−773.
(10) Wu, Q.; Xiong, S.; Shen, P.; Zhao, S.; Li, Y.; Su, D.; Orlov, A. Exceptional activity of sub-nm Pt clusters on CdS for photocatalytic hydrogen production: a combined experimental and first-principles study. *Catal. Sci. Technol.* **2015**, *5*, 2059−2064.
(11) Wu, Q.; Cen, J.; Zhao, Y.; Tong, X.; Li, Y.; Frenkel, A. I.; Zhao, S.; Orlov, A. A comprehensive study of catalytic, morphological and electronic properties of ligand-protected gold nanoclusters using XPS, STM, XAFS, and TPD techniques. *Phys. Chem. Chem. Phys.* **2018**, *20*, 1497−1503.
(12) Schweinberger, F. F.; Berr, M. J.; Döblinger, M.; Wolff, C.; Sanwald, K. E.; Crampton, A. S.; Ridge, C. J.; Jäckel, F.; Feldmann, J.; Tschurl, M.; Heiz, U. Cluster Size Effects in the Photocatalytic Hydrogen Evolution Reaction. *J. Am. Chem. Soc.* **2013**, *135*, 13262−13265.
(13) Wu, Q.; Ridge, C. J.; Zhao, S.; Zakharov, D.; Cen, J.; Tong, X.; Connors, E.; Su, D.; Stach, E. A.; Lindsay, C. M.; Orlov, A. Development of a New Generation of Stable, Tunable, and Catalytically Active Nanoparticles Produced by the Helium Nano-droplet Deposition Method. *J. Phys. Chem. Lett.* **2016**, *7*, 2910−2914.
(14) Dong, A.; Ye, X.; Chen, J.; Kang, Y.; Gordon, T.; Kikkawa, J. M.; Murray, C. B. A Generalized Ligand-Exchange Strategy Enabling Sequential Surface Functionalization of Colloidal Nanocrystals. *J. Am. Chem. Soc.* **2011**, *133*, 998−1006.
(15) Kang, Y.; Murray, C. B. Synthesis and Electrocatalytic Properties of Cubic Mn−Pt Nanocrystals (Nanocubes). *J. Am. Chem. Soc.* **2010**, *132*, 7568−7569.
(16) Nishihata, Y.; Mizuki, J.; Akao, T.; Tanaka, H.; Uenishi, M.; Kimura, M.; Okamoto, T.; Hamada, N. Self-regeneration of a Pd-perovskite catalyst for automotive emissions control. *Nature* **2002**, *418*, 164−167.
(17) Tanaka, H.; Taniguchi, M.; Uenishi, M.; Kajita, N.; Tan, I.; Nishihata, Y.; Mizuki, J. i.; Narita, K.; Kimura, M.; Kaneko, K. Self-Regenerating Rh- and Pt-Based Perovskite Catalysts for Automotive-Emissions Control. *Angew. Chem.* **2006**, *118*, 6144−6148.
(18) Kato, H.; Sasaki, Y.; Shirakura, N.; Kudo, A. Synthesis of highly active rhodium-doped SrTiO3 powders in Z-scheme systems for visible-light-driven photocatalytic overall water splitting. *J. Mater. Chem. A* **2013**, *1*, 12327−12333.
(19) Jia, Q. X.; Iwase, A.; Kudo, A. BiVO4-Ru/SrTiO3: Rh composite Z-scheme photocatalyst for solar water splitting. *Chem. Sci.* **2014**, *5*, 1513−1519.
(20) Cen, J.; Wu, Q.; Yan, D.; Tao, J.; Kisslinger, K.; Liu, M.; Orlov, A. Photoelectrochemical water splitting with a SrTiO3:Nb/SrTiO3 n +-n homojunction structure. *Phys. Chem. Chem. Phys.* **2017**, *19*, 2760−2767.
(21) Yan, B.; Yang, X.; Yao, S.; Wan, J.; Myint, M.; Gomez, E.; Xie, Z.; Kattel, S.; Xu, W.; Chen, J. G. Dry Reforming of Ethane and Butane with CO2 over PtNi/CeO2 Bimetallic Catalysts. *ACS Catal.* **2016**, *6*, 7283−7292.
(22) Wu, Q.; Cen, J.; Goodman, K. R.; White, M. G.; Ramakrishnan, G.; Orlov, A. Understanding the Interactions of CO2 with Doped and Undoped SrTiO3. *ChemSusChem* **2016**, *9*, 1889−1897.
(23) Niishiro, R.; Tanaka, S.; Kudo, A. Hydrothermal-synthesized SrTiO3 photocatalyst codoped with rhodium and antimony with visible-light response for sacrificial H-2 and O-2 evolution and application to overall water splitting. *Appl. Catal., B* **2014**, *150*, 187−196.
(24) Beale, A. M.; Weckhuysen, B. M. EXAFS as a tool to interrogate the size and shape of mono and bimetallic catalyst nanoparticles. *Phys. Chem. Chem. Phys.* **2010**, *12*, 5562−5574.
(25) Van Hardeveld, R.; Hartog, F. The statistics of surface atoms and surface sites on metal crystals. *Surf. Sci.* **1969**, *15*, 189−230.
(26) Williams, W. D.; Shekhar, M.; Lee, W.-S.; Kispersky, V.; Delgass, W. N.; Ribeiro, F. H.; Kim, S. M.; Stach, E. A.; Miller, J. T.; Allard, L. F. Metallic Corner Atoms in Gold Clusters Supported on Rutile Are the Dominant Active Site during Water−Gas Shift Catalysis. *J. Am. Chem. Soc.* **2010**, *132*, 14018−14020.
(27) Shekhar, M.; Wang, J.; Lee, W.-S.; Williams, W. D.; Kim, S. M.; Stach, E. A.; Miller, J. T.; Delgass, W. N.; Ribeiro, F. H. Size and Support Effects for the Water−Gas Shift Catalysis over Gold Nanoparticles Supported on Model Al2O3 and TiO2. *J. Am. Chem. Soc.* **2012**, *134*, 4700−4708.
(28) Matsubu, J. C.; Yang, V. N.; Christopher, P. Isolated Metal Active Site Concentration and Stability Control Catalytic CO2 Reduction Selectivity. *J. Am. Chem. Soc.* **2015**, *137*, 3076−3084.
(29) Yang, C.; Garl, C. W. Infrared Studies of Carbon Monoxide Chemisorbed on Rhodium. *J. Phys. Chem.* **1957**, *61*, 1504−1512.
(30) Demiroglu, I.; Li, Z. Y.; Piccolo, L.; Johnston, R. L. A DFT study of molecular adsorption on Au-Rh nanoalloys. *Catal. Sci. Technol.* **2016**, *6*, 6916−6931.
(31) Woerner, W. R.; Plonka, A. M.; Chen, X.; Banerjee, D.; Thallapally, P. K.; Parise, J. B. Simultaneous in Situ X-ray Diffraction and Calorimetric Studies as a Tool To Evaluate Gas Adsorption in Microporous Materials. *J. Phys. Chem. C* **2016**, *120*, 360−369.
(32) Frenkel, A. I.; Hills, C. W.; Nuzzo, R. G. A View from the Inside: Complexity in the Atomic Scale Ordering of Supported Metal Nanoparticles. *J. Phys. Chem. B* **2001**, *105*, 12689−12703.
(33) Ravel, B.; Newville, M. ATHENA, ARTEMIS, HEPHAESTUS: data analysis for X-ray absorption spectroscopy using IFEFFIT. *J. Synchrotron Radiat.* **2005**, *12*, 537−541.
(34) Newville, M. IFEFFIT: interactive XAFS analysis and FEFF fitting. *J. Synchrotron Radiat.* **2001**, *8*, 322−324.

DOI: 10.1021/acs.chemmater.7b04699
Chem. Mater. 2018, 30, 1585−1592